Journal of Computational Physics 228 (2009) 2426–2442

Contents lists available at ScienceDirect

Journal of Computational Physics

journal homepage: www.elsevier.com/locate/jcp

A high-order incompressible flow solver with WENO

Ju Zhang *, Thomas L. Jackson

Computational Science and Engineering, University of Illinois at Urbana-Champaign, 3243 Digital Computer Laboratory, 1304 West Springfield Avenue, Urbana, IL 61801, USA

ARTICLE INFO

Article history:
Received 24 June 2008
Received in revised form 26 September 2008
Accepted 6 December 2008
Available online 24 December 2008

Keywords:
WENO scheme
Incompressible
Methods: numerical

ABSTRACT

A numerical method for solving the incompressible Navier–Stokes equations with a 5th-order weighted essentially non-oscillatory (WENO) scheme is presented. The method is not based on artificial compressibility and is free of tunable parameters such as the artificial compressibility parameter. The method makes use of the fractional-step method in conjunction with the low-dissipation and low-dispersion Runge–Kutta (LDDRK) scheme to improve temporal accuracy of the scheme. The use of a WENO scheme makes it possible to obtain stable solutions for discontinuous initial data and resolve difficult applications with strong shear such as Kelvin–Helmholtz instability or turbulence. Good convergence rate is established for the velocity variables and numerical solutions of the present method compare well with exact solutions and other numerical results.

1. Introduction

In this paper we present a numerical method for solving the time-dependent incompressible Navier–Stokes equations. Numerical solutions of the incompressible flow equations are traditionally obtained using either SIMPLE-type pressure correction methods [30,21,5] or projection methods [8,23,4,6,14,26,15]. There are also methods that make use of the streamfunction and vorticity variables (see e.g., [2,3,29]). While the streamfunction and vorticity method has its attractive features such as the absence of the pressure variable and less equations to solve, the major disadvantage is that it is difficult to extend to three-dimensions. In addition, the vorticity at a wall boundary is often difficult to specify. The iterative approach of SIMPLE-type pressure correction methods can be extended to three-dimensions yet the computational cost is relatively high compared to that of projection methods which have been largely extended and studied for several decades.

For smooth or low Reynolds number flows, simple second order central spatial schemes (see e.g., [16,8,23,32]) perform reasonably well. However, for high Reynolds number flows or flows with strong shear, an upwinding scheme has to be applied. A variety of approaches have been developed in the past to extend the schemes for compressible flows to incompressible ones including artificial compressibility scheme [8,25], the Gudonov-like scheme [4], the ENO scheme [11], and the WENO scheme [7,34], to name a few. The main issue for the schemes based on artificial compressibility is the high stiffness for unsteady problem. The WENO scheme was also incorporated through the means of artificial compressibility in [7] so even though it improved the accuracy in the spatial discretization it still suffers the stiffness of the system when the artificial compressibility has to be minimized. In addition, there is always the question of what is the best choice of the tunable artificial compressibility parameter which may also be problem dependent. As the applications become more and more demanding in terms of the accuracy of the scheme, the second order Gudonov-like scheme may become inadequate. Pseudospectral methods as in [22,28] are highly accurate and have been applied to turbulent problems with success. However, the difficulty with pseudospectral methods lies in the limitation to relatively simple geometries and to periodic and wall boundaries. Higher

* Corresponding author. Tel.: +1 217 265 7582.
E-mail address: juzhang@uiuc.edu (J. Zhang).

0021-9991/$ - see front matter © 2008 Elsevier Inc. All rights reserved.
doi:10.1016/j.jcp.2008.12.009

order compact (HOC) central schemes [24,27] can be an alternative for higher order spatial discretization. However, as there is no built-in upwinding, it is prone to numerical oscillations especially near a discontinuity. Filtering has to be applied often. Moreover, since compact schemes involve global rather than nearby-point stencils, extra care has to be taken when parallelizing the schemes.

In the present work, we are mainly concerned with the proper spatial discretization of the convective terms with high-order schemes. We explore a simple straight-forward way of applying the 5th-order WENO scheme [19] to the incompressible Navier–Stokes equations without flux splitting that was used in [34]. The primary novelty of the method as compared to that in [7] is that the WENO scheme is applied to the convective terms without invoking the usual local characteristics and introducing artificial compressibility. Upwinding is guaranteed and the scheme can readily be used in applications involving high Reynolds number flows or flows with strong shear or even a discontinuity. The temporal scheme is based on the fractional-step scheme [23] in conjunction with the optimized two step alternating 4-6 low-dissipation and low-dispersion Runge–Kutta (LDDRK) scheme [18] to improve temporal accuracy of the scheme. To improve the accuracy in the spatial discretization of the viscous terms, a 6th-order compact scheme of [24] is applied. The limitation of compact schemes in approximating the convective terms in problems involving strong shear will also be demonstrated in this paper.

2. Numerical method

The nondimensionalised Navier–Stokes and continuity equations to be solved for incompressible viscous flows are

$$\frac{\partial u_i}{\partial t} + u_j \frac{\partial u_i}{\partial x_j} = -\frac{\partial p}{\partial x_i} + \frac{1}{Re}\frac{\partial^2 u_i}{\partial x_j \partial x_j}, \tag{1}$$

$$\frac{\partial u_i}{\partial x_i} = 0, \tag{2}$$

where Re is the Reynolds number, p the pressure, and u_i the velocity components.

The temporal scheme is based on the fractional-step method of [23], with slight modifications, and in conjunction with a low-dissipation and low-dispersion Runge–Kutta (LDDRK) scheme [18]. For completion, the basic fractional-step scheme during each Runge–Kutta stage is given by

$$\frac{\widehat{u}_i - u_i^n}{\Delta t} = -H_i^n + \frac{1}{Re}\left(\frac{\delta^2}{\delta x_1^2} + \frac{\delta^2}{\delta x_2^2} + \frac{\delta^2}{\delta x_3^2}\right) u_i^n, \tag{3}$$

$$\frac{u_i^{n+1} - \widehat{u}_i}{\Delta t} = -G(p^{n+1}). \tag{4}$$

with

$$D(u_i^{n+1}) = 0, \tag{5}$$

where $H_i^n = u_j \frac{\partial u_i}{\partial x_j}$ is the convective terms, $\delta/\delta x_i$ represents discrete finite difference operators and G and D represent discrete gradient and divergence operators, respectively. Since the Runge–Kutta method is used, no additional special temporal scheme, such as the Adam–Bashforth method is applied to the convective terms. Also, note that the current target applications are moderate to high Reynolds number flows, so no implicit treatment to the viscous terms, like the Crank–Nicolson scheme, is found necessary. Therefore, no implicit solver for $\widehat{u}_i$ is needed and the variable p in Eq. (4) is pressure itself as opposed to the ϕ variable as in [23]. This difference turns out to be critical and advantageous as discussed by [12] in achieving higher order of accuracy in solving for pressure. The Runge–Kutta scheme can be easily applied by treating the entire RHS of Eq. (3) as the slope. The optimized two step 4–6 alternating LDDRK scheme in [18] is chosen in this work. A Poisson solve for pressure using MUDPACK [1] is performed at the end of each Runge–Kutta stage.

A variant of the staggered mesh of [16] is used as depicted in Fig. 1. The cell corners are represented by circles and the centers of the faces are denoted by crosses in the figure. The pressure variable is defined at the corners of each cell, and the velocity variables on the faces that are parallel to their directions, e.g., u and v are defined on horizontal and vertical edges of the cell in two dimensions, respectively. The mesh is staggered in this way so that a no-slip boundary condition can be more conveniently imposed. Of course, if the wall-normal velocity needs to be specified more conveniently, the mesh can always be staggered in the original way [16]. As already mentioned in the introduction, the spatial discretization of the convective terms H_i^n is the 5th-order WENO scheme [19]. Typically, artificial compressibility is introduced to the scheme when extending the schemes developed for compressible flows such as WENO to incompressible one [7]. In the present work, a straight-forward application of the 5th-order finite difference WENO scheme to the convective terms is explored and verified. In a similar spirit of applying ENO to the incompressible Navier–Stokes equation [11], the natural implementation of upwinding is to use the signs of the velocities in front of the derivatives $\frac{\partial u_i}{\partial x_j}$ in the convective terms in Eq. (1) at appropriate locations, and to apply WENO equation by equation. For completion, let f be the velocity components u_i in Eq. (1), the reconstruction of f along the directions of u_j in the convective terms is based on the 5th-order WENO scheme and can be expressed as

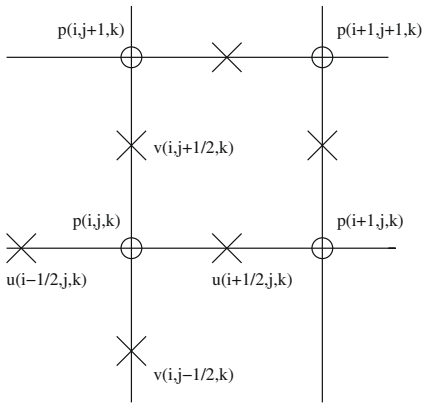

Fig. 1. The staggered mesh in two dimensions. Note that the cell corners are represented by circles and the centers of cell faces are denoted by crosses.

$$\hat{f}_{j+1/2} = \sum_{k=1}^{3} \omega_k \hat{f}^k_{j+1/2},$$

where $\hat{f}^k_{j+1/2}$ is a second order polynomial reconstruction of f on the kth set of stencils and the nonlinear weights ω_k are

$$\omega_k = \widetilde{\omega_k} / \sum_{l=1}^{3} \widetilde{\omega_l}, \widetilde{\omega_l} = \frac{\gamma_l}{(\epsilon + \beta_l)^2}. \tag{6}$$

As mentioned above, upwinding can be naturally determined by the signs of velocities in the convective terms. For the calculation of $\hat{f}^k_{j+1/2}$, we use $u_{j+1/2}$ which is simply averaged from its neighbors to determine upwinding. If $u_{j+1/2} \geqslant 0$, we have $\gamma_1 = 0.3, \gamma_2 = 0.6, \gamma_3 = 0.1$, and $\hat{f}^k_{j+1/2}$ can be computed as

$$\begin{aligned}
\hat{f}^1_{j+1/2} &= \frac{1}{3} f_j + \frac{5}{6} f_{j+1} - \frac{1}{6} f_{j+2}, \\
\hat{f}^2_{j+1/2} &= -\frac{1}{6} f_{j-1} + \frac{5}{6} f_j + \frac{1}{3} f_{j+1}, \\
\hat{f}^3_{j+1/2} &= \frac{1}{3} f_{j-2} - \frac{7}{6} f_{j-1} + \frac{11}{6} f_j,
\end{aligned}$$

with the smoothness indicators β_l given by

$$\begin{aligned}
\beta_1 &= \frac{13}{12}(f_j - 2f_{j+1} + f_{j+2})^2 + \frac{1}{4}(3f_j - 4f_{j+1} + f_{j+2})^2, \\
\beta_2 &= \frac{13}{12}(f_{j-1} - 2f_j + f_{j+1})^2 + \frac{1}{4}(f_{j-1} - f_{j+1})^2, \\
\beta_3 &= \frac{13}{12}(f_{j-2} - 2f_{j-1} + f_j)^2 + \frac{1}{4}(f_{j-2} - 4f_{j-1} + 3f_j)^2.
\end{aligned}$$

For $u_{j+1/2} < 0$, we have $\gamma_1 = 0.1, \gamma_2 = 0.6, \gamma_3 = 0.3$, and the formulations for $\hat{f}^k_{j+1/2}$ and the smoothness indicators become

$$\begin{aligned}
\hat{f}^1_{j+1/2} &= \frac{11}{6} f_{j+1} - \frac{7}{6} f_{j+2} + \frac{1}{3} f_{j+3}, \\
\hat{f}^2_{j+1/2} &= \frac{1}{3} f_j + \frac{5}{6} f_{j+1} - \frac{1}{6} f_{j+2}, \\
\hat{f}^3_{j+1/2} &= -\frac{1}{6} f_{j-1} + \frac{5}{6} f_j + \frac{1}{3} f_{j+1},
\end{aligned}$$

and

$$\begin{aligned}
\beta_1 &= \frac{13}{12}(f_{j+1} - 2f_{j+2} + f_{j+3})^2 + \frac{1}{4}(3f_{j+1} - 4f_{j+2} + f_{j+3})^2, \\
\beta_2 &= \frac{13}{12}(f_j - 2f_{j+1} + f_{j+2})^2 + \frac{1}{4}(f_j - f_{j+2})^2, \\
\beta_3 &= \frac{13}{12}(f_{j-1} - 2f_j + f_{j+1})^2 + \frac{1}{4}(f_{j-1} - 4f_j + 3f_{j+1})^2.
\end{aligned}$$

Finally, ϵ is set to 10^{-6} to avoid divisions by zero in the calculations of the smoothness indicators. To summarize, the derivatives $\frac{\partial u_i}{\partial x_j}$ in the convective terms $u_j \frac{\partial u_i}{\partial x_j}$ are approximated with exactly the same procedure as that for the derivative of a scalar

in [19]. The upwinding is determined by the signs of the velocities in front of the derivatives $\frac{\partial u_i}{\partial x_j}$ at appropriate locations. It is worthwhile to point out that, as long as the divergence constraint, namely Eq. (2), is satisfied well by refining the grid resolution, the current scheme can be reasonably conservative for relatively smooth problems (see Section 3.3). The advantage of using the non-conservative form as opposed to the conservative form is given in the Discussion section. As mentioned in the introduction section, an alternative high-order discretization scheme for the convective terms is the high-order compact (HOC) scheme. The staggered 6th-order compact scheme in [27] is also implemented and compared to the WENO scheme here. An obvious advantage of the current approach using WENO is that it is easier to implement and parallelize than compact schemes which involve global rather than nearby-point stencils as in the WENO scheme. Unlike the convective terms, the viscous terms can be approximated by higher order central schemes without problems. In fact, the 6th-order compact scheme in [24] is chosen here for the spatial discretization of the viscous terms to achieve higher accuracy. For periodic boundary conditions, a slightly perturbed form of the tridiagonal system needs to be solved for the compact schemes:

$$\begin{bmatrix} b_1 & c_1 & & & a_1 \\ a_2 & b_2 & c_2 & & \\ & a_3 & b_3 & \cdot & \\ & & \cdot & \cdot & c_{n-1} \\ c_n & & & a_n & b_n \end{bmatrix} \begin{bmatrix} x_1 \\ x_2 \\ \cdot \\ \cdot \\ x_n \end{bmatrix} = \begin{bmatrix} d_1 \\ d_2 \\ \cdot \\ \cdot \\ d_n \end{bmatrix}.$$

We make use of the Sherman–Morrison formula to avoid the additional operations of Gaussian elimination and still use the Thomas algorithm. The system to be solved is now

$$(A + uv^T)x = d$$

where

$$A = \begin{bmatrix} 0 & c_1 & & & 0 \\ a_2 & b_2 & c_2 & & \\ & a_3 & b_3 & \cdot & \\ & & \cdot & \cdot & c_{n-1} \\ 0 & & & a_n & b_n - (a_1/b_1)c_n \end{bmatrix},$$

$$u^T = [b_1 0 0 \ldots 0 c_n],\ v^T = [1 0 0 \ldots 0 a_1/b_1].$$

The solution is then obtained as

$$x = y - (v^T y)/(1 + (v^T q))q$$

where x and q are obtained by solving

$$Ay = d, Aq = u$$

with the Thomas algorithm applied to the 3rd to the nth row of A, and after $[x_3, \ldots, x_n]$ are obtained, x_1 and x_2 can be easily calculated from the first two rows of A.

Finally, for the discretization of the pressure solve, the divergence of the intermediate velocity at the corners of each cell (where the pressure variable is defined) is approximated by

$$D(\hat{\mathbf{u}}) = \frac{1}{\Delta x}\left(\hat{u}_{i+\frac{1}{2}j} - \hat{u}_{i-\frac{1}{2}j}\right) + \frac{1}{\Delta y}\left(\hat{v}_{ij+\frac{1}{2}} - \hat{v}_{ij-\frac{1}{2}}\right),$$

and the discrete operator for the second order elliptic operator is given by

$$DG(p_{ij}) = \frac{p_{i+1,j} - 2p_{ij} + p_{i-1,j}}{(\Delta x)^2} + \frac{p_{ij+1} - 2p_{ij} + p_{ij-1}}{(\Delta y)^2}. \tag{7}$$

3. Numerical results

3.1. Taylor–Green vortex test

The Taylor–Green vortex test problem has been widely used for verification purpose for incompressible viscous flow solvers. It is also used here to establish the order of accuracy of the method. The 2D exact solution to the unsteady problem is given by

$$u(x,y,t) = -\cos(kx)\sin(ky)exp(-2k^2t/Re),$$
$$v(x,y,t) = \sin(kx)\cos(ky)exp(-2t^2/Re),$$
$$p(x,y,t) = -\frac{1}{4}(cos(kx) + cos(ky))exp(-4k^2t/Re);$$

a solution to the Navier–Stokes and continuity equations. The numerical solutions are computed on a square domain of side 2π with periodic boundary conditions in both x and y-direction.

We establish the formal order of accuracy of our scheme in space by running a $Re = 100$ Taylor–Green vortex with $k = 4$ for 100 steps with a fixed time step of 0.001. Three different resolutions with 32^2, 64^2 and 128^2 uniform grid points are used in the study. Table 1 shows the convergence rate of the scheme. A convergence rate of better than 3rd-order is clearly seen for the velocity variables while that for pressure is essentially 2nd-order. It is quite remarkable that the full 2nd-order accuracy of the discretization of the elliptic operator (Eq. 7) in the pressure Poisson solve is achieved. This is expected as our temporal discretization is explicit and is essentially equivalent to the Gauge method by [12].

Table 1
Maximum error after 100 time steps for TG test. dt = 0.001. The errors and convergence rates in u-velocity for $Re = 1e6$ and advecting $Re = 100$ TG vortex are also shown in the bottom two rows.

Variables	32	Rate	64	Rate	128
u	$3.32e-3$	3.44	$3.06e-4$	4.47	$1.38e-5$
v	$3.32e-3$	3.44	$3.06e-4$	4.48	$1.37e-5$
p	$3.98e-2$	2.36	$7.76e-3$	1.87	$2.12e-3$
$\|\nabla p\|$	$8.90e-1$	1.83	$2.50e-1$	1.94	$6.50e-2$
$Re = 1e6$	$3.56e-3$	3.39	$3.39e-4$	4.51	$1.49e-5$
Advecting	$1.98e-2$	4.09	$1.16e-3$	4.83	$4.07e-5$

Table 2
Maximum absolute error of velocity component u in numerical solutions of the two-dimensional Taylor–Green flow. The HOC results are from Pandit et al. [29].

Time	WENO	Sixth-order compact	HOC of [29]
$t = 1$	$2.98e-5$	$2.82e-6$	$2.19e-2$
$t = 10$	$2.12e-4$	$8.59e-6$	$1.87e-2$

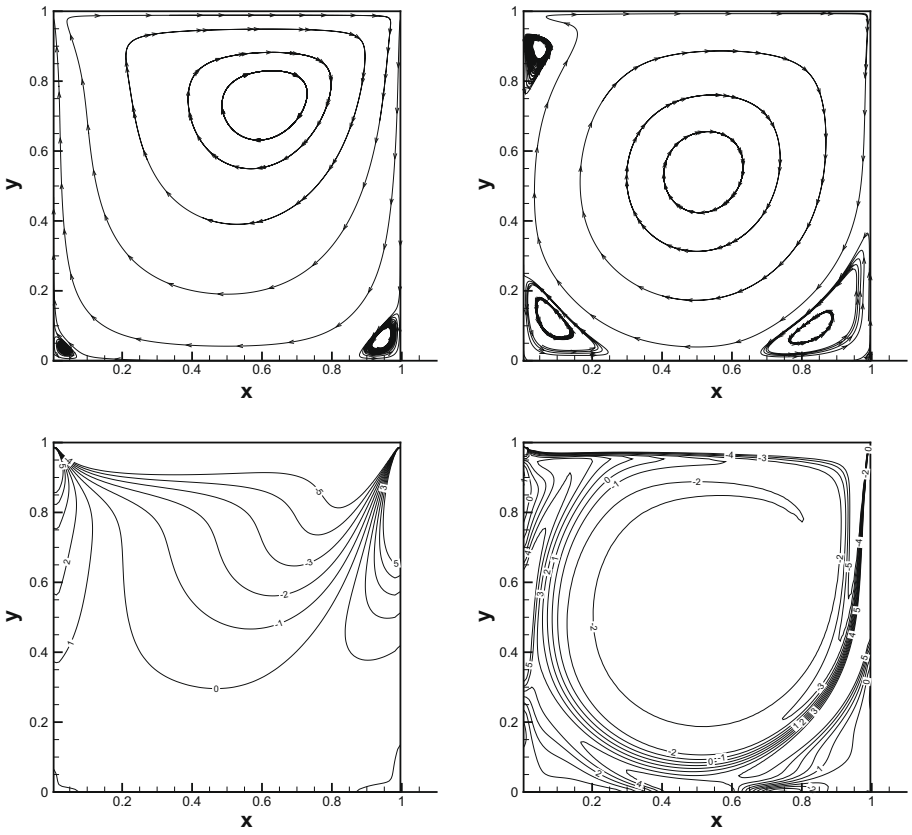

Fig. 2. Streamlines (top panels) and vorticity (bottom panels) of driven cavity for $Re = 100$ (left panels) and 3200 (right panels). The grid resolution is 128×128 and time step is 0.001.

The effect of one parameter worth to examine is ϵ in the nonlinear weights ω_k (Eq. 6) of the WENO scheme as it was found that the values of ϵ may alter the convergence rate of the scheme in the one-dimensional problems examined in [17]. Three more values of ϵ, namely 10^{-4}, 10^{-12} and 10^{-16}, in addition to the standard value of 10^{-6} are checked here and the results are basically insensitive to the values of ϵ. Therefore, the standard value of 10^{-6} is used throughout this paper. The accuracy in our problem is presumably limited by the 2nd-order Poisson solve and not by the subtleties such as the value of ϵ. This points to the possible future improvement by implementing the solutions proposed in [6,20] in addition to that for the nonlinear weights in WENO proposed in [17]. A deferred correction method was actually used in [20]. Finally, the gradient of pressure also seems to converge at a second order rate as seen in the table.

To demonstrate the robustness of the current scheme, a high *Re* of 1e6 and an advecting (with background velocity of (U,V) = (1,1)) Taylor–Green vortex are simulated and the maximum absolute errors in *u*-velocity are shown to also converge at a rate better than 3rd-order in the bottom two rows of Table 1. The convergence behaviors of other variables are similar to those of the reference case of $Re = 100$ and $k = 4$.

We do recognize that for smooth problems like the Taylor–Green vortex, the performance of high-order compact schemes can be better than the WENO scheme as can be seen in the following test. The same Taylor–Green vortex at $Re = 100$ and $k = 1$ with a grid of 32×32 and a time step of 0.01 is simulated with both WENO and the staggered 6th-order compact scheme of [27], and the errors are compared in Table 2. It is seen that, due to its spectral like resolution, the compact scheme does perform remarkably better than the WENO scheme for this test. However, it should be pointed out that this is probably only true for smooth problems, like the Taylor–Green vortex. For more difficult applications, like the ones with strong shear or discontinuities, the WENO scheme will perform much better than compact schemes as will be illustrated in Section 3.3 and in Discussion section. In addition, the current scheme equipped with WENO and Runge–Kutta scheme does seem to perform better than some of the recent high-order schemes. For example, Table 2 also lists the errors in the HOC scheme of [29]

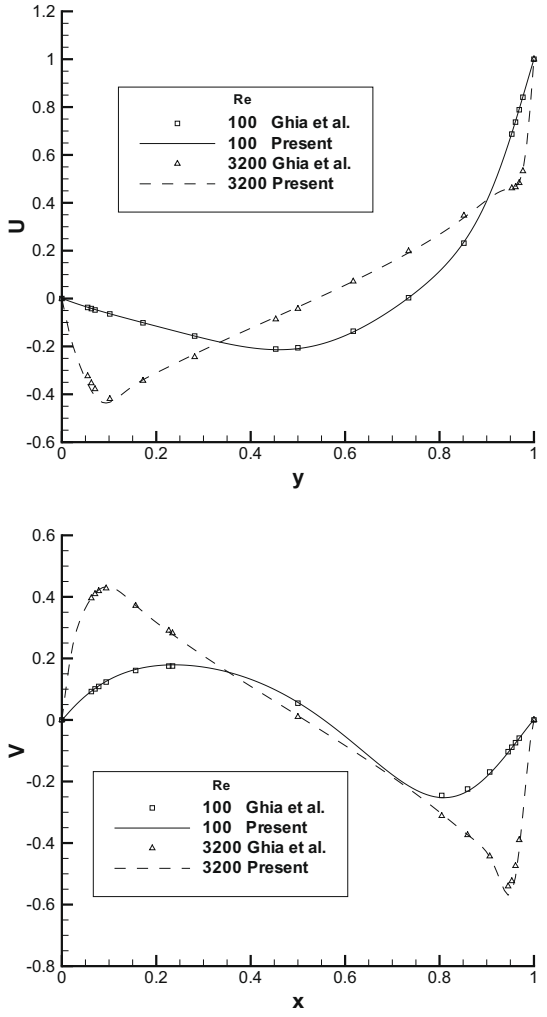

Fig. 3. Comparison of velocity profiles of driven cavity test problem.

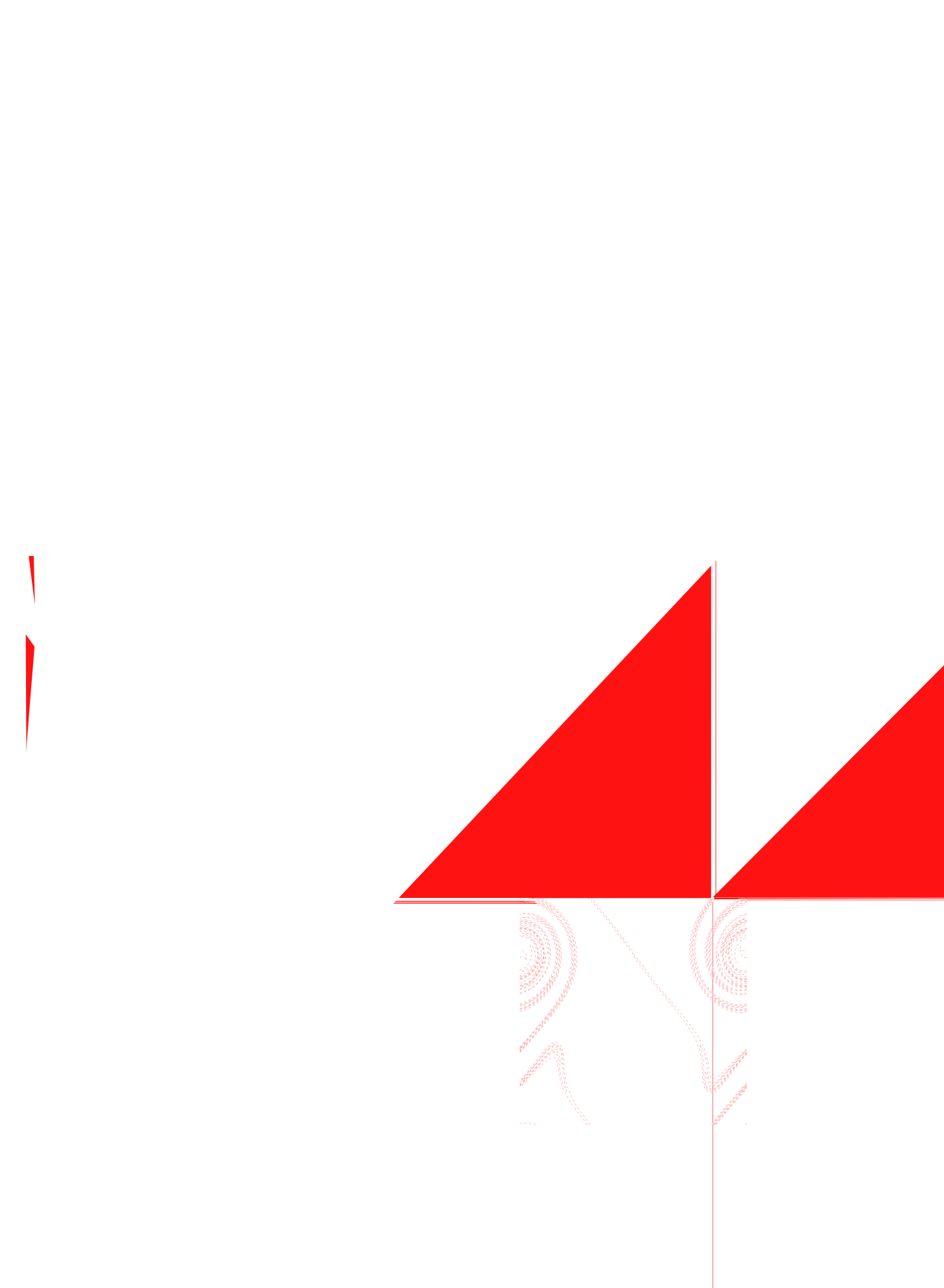

provides a stringent test when $\rho \to 0$. Unlike in the TG and driven cavity tests, if the convective terms are not treated with upwinding, numerical oscillations will occur in this kind of test with strong shear.

To compare with the results by Bell et al. [4], we first run the inviscid test with $\rho = 1/30$ and $\delta = 0.25$ on the same sets of grid as in [4], i.e., 128^2, 256^2 and 512^2, and with the same time step that corresponds to a CFL of 0.5. The similarity in the development of the flow features are seen for all the grids. Here, we only show the vorticity contours on 256^2 grid in Fig. 4 from $t = 0.4$ to 1.8 for comparison. This corresponds to Fig. 2 in [4]. The evolution and flow patterns look quite similar to those of [4]. Also, like in [4], there is no obvious evidence of problems with large dispersive errors in the presence of large gradients, such as oscillations or distortions in the shape of the large vorticies. The kinetic energy as defined by

$$K = \int U \cdot U \, dxdy$$

is plotted in Fig. 5 and should be compared to Fig. 4 in [4]. Instead of converging at a rate of second order as in [4], the kinetic energy is converging at a 4th-order rate in our scheme as expected. It is also quite remarkable that K in the current scheme remains essentially invariant for longer duration than that of [4]. For example, the bottom panel of Fig. 5 is plotted with the same scale as the bottom left panel of Fig. 4 in [4] and it is seen that K is essentially invariant for 512×512 case upto $t \sim 1.2$ here whereas that of [4] keeps decreasing appreciably. We suggest that the conservation error observed here is presumably due to the numerical dissipation in the scheme when large gradients are developed as seen in the evolution of the shear at late time. The numerical dissipation can be appreciated more easily in the simple one-dimensional example shown in Fig. 12 in the Discussion section. Nonetheless, the scheme is reasonably conservative in practice at the early time when the gradients in the flow are not too large yet. The conservation can also be improved by refining the grid resolution as seen in Fig. 5 so that the divergence constraint dictated by Eq. (2) is satisfied better. It is also worthwhile to present the solutions at coarser

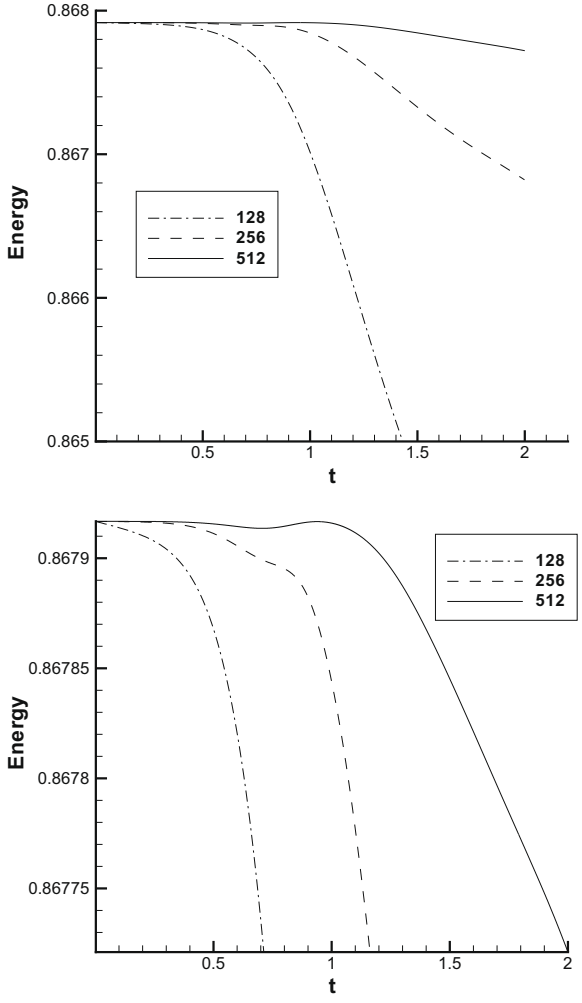

Fig. 5. Kinetic energy as a function of time for the inviscid shear layer with $\rho = 1/30$. Bottom panel is the enlarged view of the top panel.

resolutions to demonstrate the reasonable approximations by our scheme at these resolutions. These are shown in Fig. 6 where the solutions at $t = 1.8$ corresponding to the last panel in Fig. 4 are plotted for grids of 32^2, 64^2 and 128^2. The number, shape and location of the major vorticies are seen to be reasonably preserved and no spurious vorticies are seen.

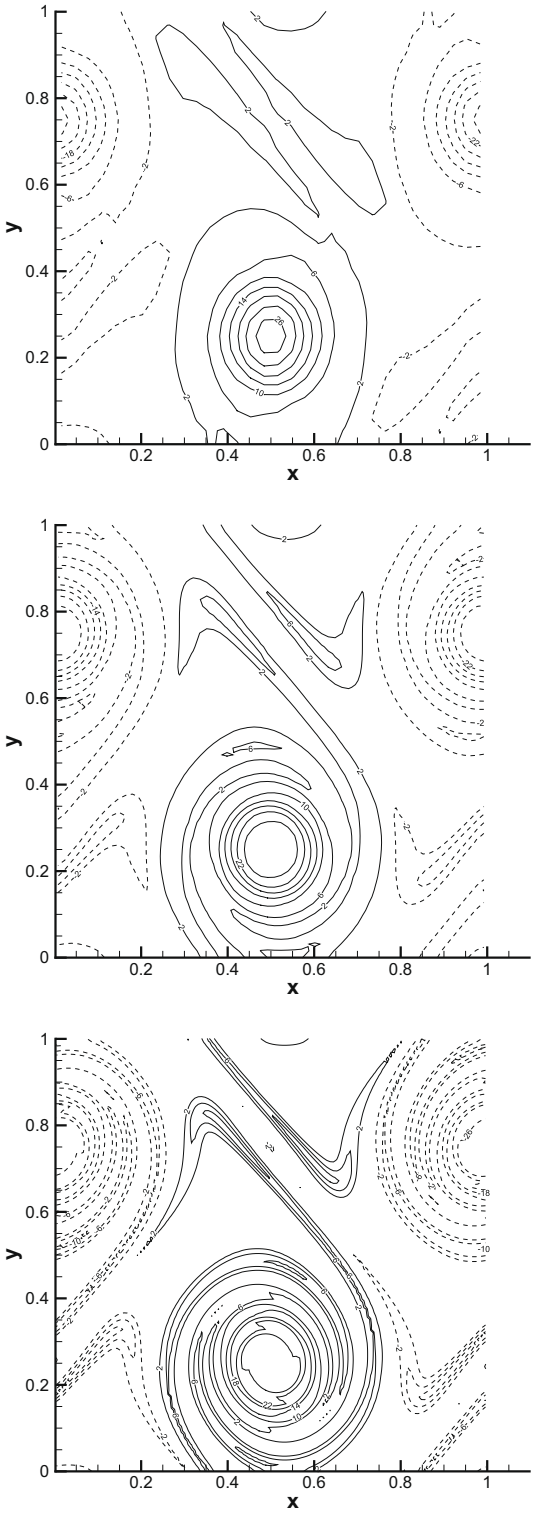

Fig. 6. Vorticity contours at $t = 1.8$ (corresponding to the last panel of Fig. 4) for the inviscid shear layer with $\rho = 1/30$ on, from top to bottom, 32×32, 64×64 and 128×128 grid, respectively.

Kinetic energy based on the perturbational velocities

$$u'(x,y,t) = u(x,y,t) - u_0(x,y),$$
$$v'(x,y,t) = v(x,y,t),$$

where $u_0(x,y)$ is the initial u-velocity given by Eq. (8), is also computed and plotted in Fig. 7. The energy apparently shows an exponential growth as predicted by the linear theory [9].

To assess how HOC schemes would perform for this kind of test with strong shear without filtering, we run the same test with the staggered 6th-order compact scheme [27]. The vorticity field is shown in Fig. 8 at $t = 1.8$. Evidence of problems in the presence of large gradients, such as oscillations in the solution indeed appears. Filtering will be needed especially when the grid is coarse to fix the problem. This is beyond the scope of the current work.

We now return to our WENO scheme and the test is next computed with $\rho \to 0$ at Re of 1e4 and for Euler equations as shown in Figs. 9 and 10, respectively. These figures should be compared to the corresponding cases in Figs. 5 and 7 in [4]. Qualitative similar features, such as the number, locations and shapes of the developed vorticies, are indeed seen for $Re = 1e4$ case especially at $t = 0.6$. However, there seems to be appreciable differences in the Euler case which is probably

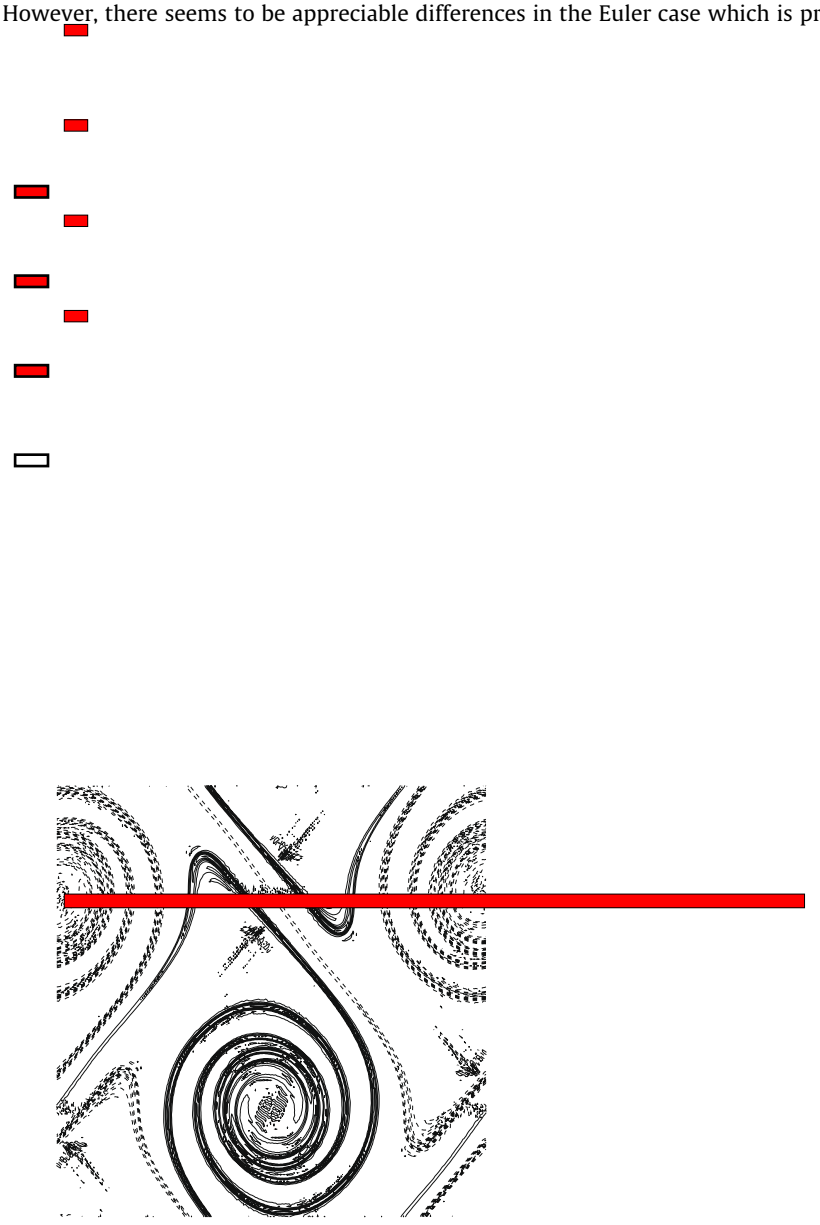

4. Discussion

To demonstrate more clearly the arguments about the accuracy and the advantage of the current WENO scheme, the common test of solving the 1D transport equation,

$$\frac{\partial f}{\partial t}+\frac{\partial f}{\partial x}=0, \tag{10}$$

is performed using the 5th-order WENO [19], the 2nd-order Gudnov-like [4], and the staggered 4th-order compact [27] schemes. The scheme for time integration is the two step 4-6 alternating LDDRK for all the spatial schemes. A step function is used as the initial profile and the boundaries are periodic. The number of grid points is 64 and the time step is 0.01. The results are compared in Fig. 12 for one period. The 5th-order WENO scheme performs well in the presence of a discontinuity as expected. The advantage of WENO being more accurate than 2nd order schemes also becomes much more clear in this simple test. The compact scheme without filtering fails to produce reasonable solution in problems involving a discontinuity as seen here or large gradients as seen in Section 3.3, and may only be good for relatively smooth problems or problems with moderate gradients.

Next, we would like to demonstrate the capability of our current WENO scheme in the direct numerical simulation (DNS) of turbulence in solid rocket motors. Tests of interest to the rocket community such as the turbulent flow in a planar periodic rocket in [31] have been carried out which will be discussed briefly here and in greater detail in a forthcoming publication. As a model of the core flow of a solid propellant rocket, the incompressible flow between parallel walls driven by injection through the walls is simulated. A multiscale asymptotic analysis similar to that used by Spalart [33] is used to treat the flow acceleration in the streamwise direction. The flow can then be homogenized and a periodic boundary condition can be used

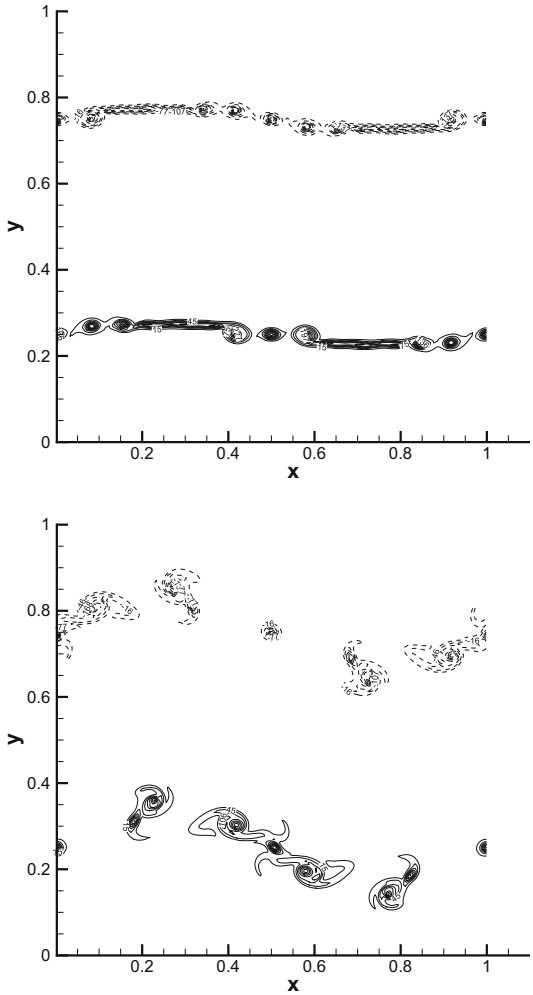

Fig. 10. Vorticity contours for shear layer with discontinuous initial condition ($\rho = 1/3e6$) on 256×256 grid at $t = 0.3$ (top) and 0.6 (bottom). Euler.

(see [31] for details). The equations to be solved are the incompressible NS equations with source terms to take into account the mass addition and acceleration due to injection

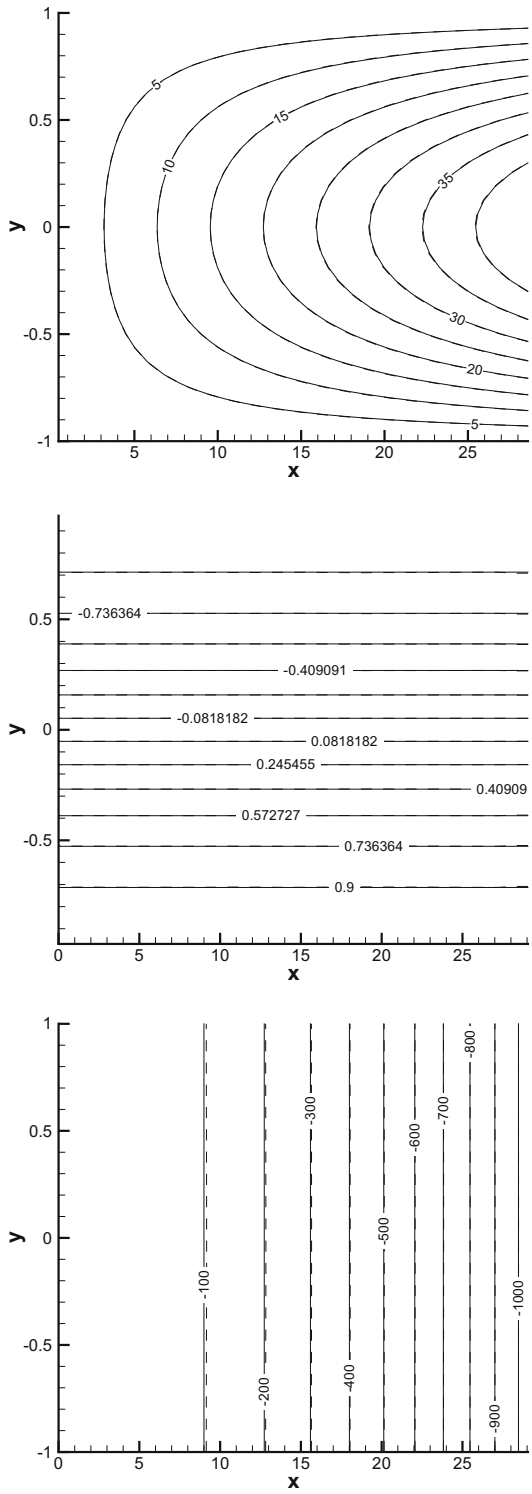

Fig. 11. Comparison of numerical solution (dashed) with Taylor/Culick's solution (solid). The u, v velocities and pressure are shown from top to bottom. The grid is 32×32 and time step is 0.001.

$$\frac{\partial u_i}{\partial x_i} = -\epsilon \bar{u}, \tag{11}$$

$$\frac{\partial u_i}{\partial t} + \epsilon u(u_i - \delta_{2i}\bar{u}_i) + u_j \frac{\partial u_i}{\partial x_j} = -\frac{\partial p}{\partial x_i} + \delta_{1i}\frac{\pi^2}{4\epsilon} + \frac{1}{Re}\frac{\partial^2 u_i}{\partial x_j \partial x_j}, \tag{12}$$

where $\epsilon = V_{inj}/U_m$ is a small parameter and is the ratio of the injected mass flow rate over the mass-averaged core flow rate, and an overbar denotes a mean quantity. The Case A in [31] corresponding to $\epsilon = 0.04$ is computed here with a uniform 256^2 grid. Fig. 13 shows the flow feature characterized by near-wall-large-scale coherent structures inclined at an angle opposite to the mean flow direction seen in [31] is reproduced here. The rms velocities shown in Fig. 14 also exhibit similarities to those in [31], e.g., the maximum of cross stream rms fluctuations is at the center of the channel while two maxima close to the walls appear for streamwise rms fluctuations. Note that the current simulation is 2D whereas that in [31] is 3D. This is the reason why the rms velocities are stronger in the current simulation due to the lack of the freedom in the spanwise direction. Also, note that the statistical sample here is not as large as that in [31] also due to the lack of the spanwise direction that can be used to improve the statistics.

Finally in this section, we would like to discuss in some detail about the conservation property of our current scheme. Because of the incompressiblity condition (Eq. 2), the Navier–Stokes equations, i.e., Eq. 1 can also be written in conservative form

$$\frac{\partial u_i}{\partial t} + \frac{\partial u_i u_j}{\partial x_j} = -\frac{\partial p}{\partial x_i} + \frac{1}{Re}\frac{\partial^2 u_i}{\partial x_j \partial x_j}, \tag{13}$$

and therefore, solved in conservative form. It has the advantage of being more conservative and less dissipative as shown by [26]. This seems to be also the case here for the shear test with $\rho = 1/30$ as shown by the kinetic energy evolution in the top panel of Fig. 15. The solution by conservative form is more conservative than that by non-conservative form in the sense that the kinetic energy is closer to being a constant. However, as the application becomes more difficult like the shear with discontinuous initial condition, the trend seems to be reverted. This is shown in the bottom panel of Fig. 15 for the inviscid $\rho = 1/3e6$ case. This is presumably due to the fact that solving in conservative form is more prone to numerical noise as also

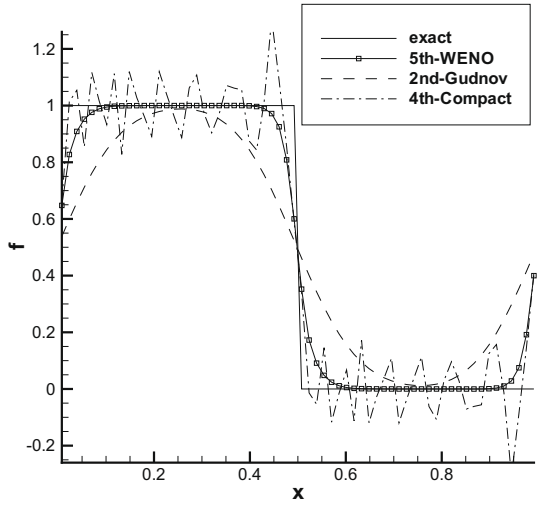

Fig. 12. Comparison of numerical solutions after one period to the exact solution of the 1D transport equation for a step function for different schemes.

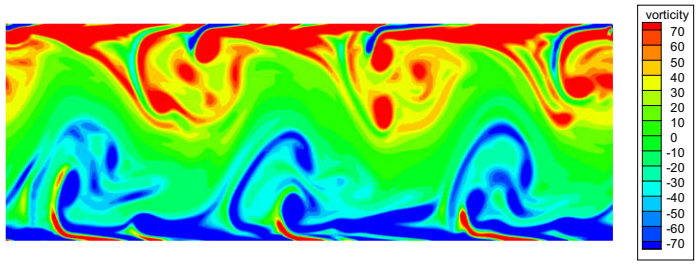

Fig. 13. Instantaneous vorticity field in planar periodic rocket.

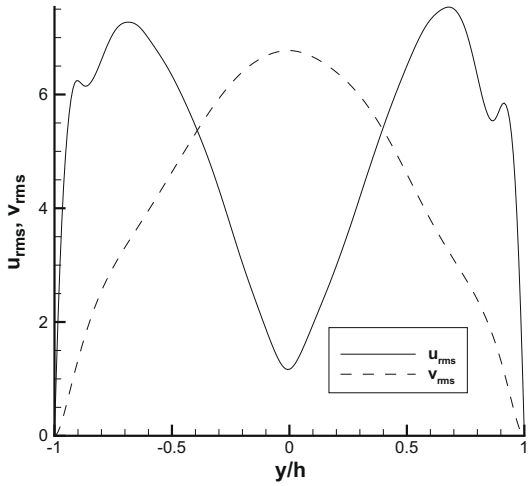

Fig. 14. Rms velocity profiles for planar periodic rocket.

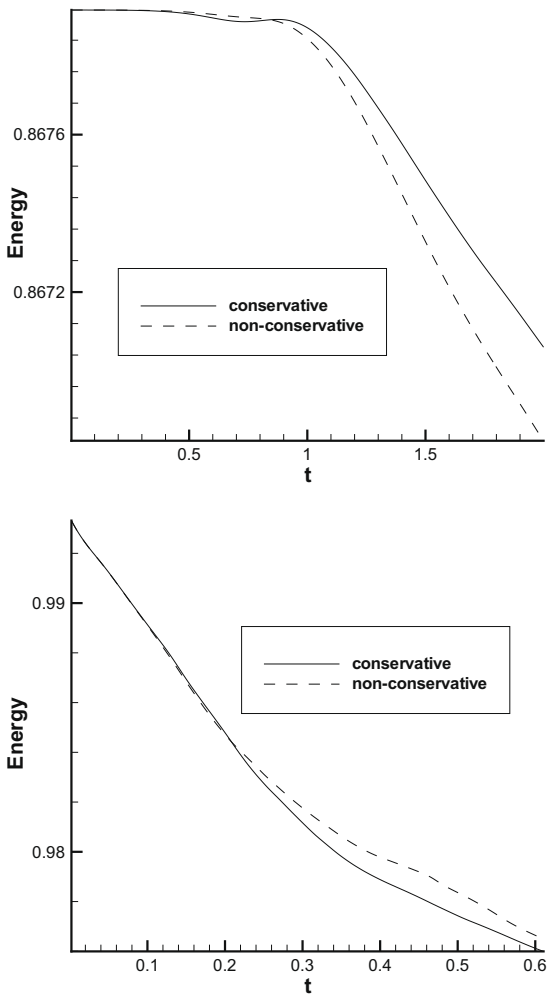

Fig. 15. Kinetic energy as a function of time for the inviscid shear layer on 256×256 grid for $\rho = 1/30$ (top) and $1/3e6$ (bottom). The solution by conservative form (Eq. 13) is plotted by solid lines while that by non-conservative form (Eqn. 1) by dashed lines.

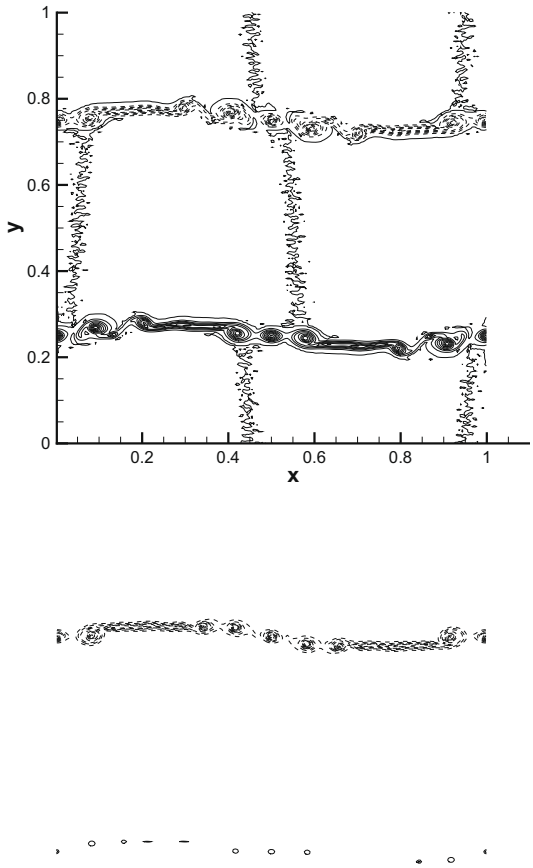

noted in [4]. It can be demonstrated by showing the zero contour lines of the vorticity where the numerical noise is most pronounced. This is shown in Fig. 16 by the comparison of the results of conservative and non-conservative schemes. These vorticity fields are at $t = 0.3$ corresponding to the two cases shown in the top panel of Fig. 10, i.e., the $\rho = 1/3e6$ case. The flowfield is substantially polluted by the numerical noise in the solution by conservative form whereas that by the non-conservative form is affected to a much less degree. The pollution in the solution by the conservative scheme also results in a practically worse conservation than its non-conservative counterpart in this case. Furthermore, the maximum error in u-velocity in the reference TG vortex test ($Re = 100$, $k = 4$) by conservative form is $5.92e-3$ which is larger than that of $3.32e-3$ by the non-conservative form as shown in Table 1. Also, the maximum errors in u-velocity in the interior flow test in Section 3.4 are $4.37e-3$ and $3.76e-3$ for the conservative and non-conservative form, respectively. Therefore, although the conservative form may have better conservation property globally when the problems are relatively smooth, it seems to have larger errors locally than the scheme with non-conservative form.

5. Conclusion

A numerical method for solving the incompressible Navier–Stokes equations with a 5th-order weighted essentially non-oscillatory (WENO) scheme was presented. The WENO scheme is applied to the convective terms in a straight-forward way without invoking artificial compressibility. This rather simple application of the WENO scheme was validated by several numerical tests with exact solutions or previous numerical results, and was shown to be close to 4th-order accurate for velocity variables. Because of the simplicity, the method is very easy to implement and parallelize especially in 3D compared to compact schemes. The use of a WENO scheme also makes it possible to resolve difficult applications with strong shear and

remain stable for even discontinuous initial data where compact schemes without filtering would generally fail. These properties are all highly desirable for a good numerical scheme to be both robust and highly accurate at the same time. A 6th-order compact scheme is used for the viscous terms to achieve a higher accuracy. Finally, to improve temporal accuracy of the scheme, the fractional-step method is equipped with the optimized two step alternating 4–6 low-dissipation and low-dispersion Runge–Kutta (LDDRK) scheme.

Acknowledgments

This work was supported by the US Department of Energy through the University of California under subcontract B523819, and by NASA Constellation University Institutes Project under Grant NCC3-989, and through the University of Maryland under subcontract Z634015, with Claudia Meyer as the project manager. This work was partially supported through Buckmaster Research under Grant FA9550-07-C-0123 under a Phase II program with the Air Force, program manager Dr. A Nachman.

References

[1] J. Adams, MUDPACK: multigrid fortran software for the efficient solution of linear elliptic partial differential equations, Appl. Math. Comput. 34 (1989) 113–146.
[2] F. Auteri, L. Quartapelle, L. Vigevano, Accurate $\psi - \zeta$ spectral solution of the singular driven cavity problem, J. Comput. Phys. 180 (2002) 597–615.
[3] E. Barragy, G.F. Carey, Stream function-vorticity driven cavity solution using p finite elements, Comput. Fluids 26 (5) (1997) 453–468.
[4] J.B. Bell, P. Colella, H.M. Glaz, A second-order projection method for the incompressible Navier–Stokes equations, J. Comput. Phys. 85 (1989) 257.
[5] H. Bijl, P. Wesseling, A unified method for computing incompressible and compressible flows in boundary-fitted coordinates, J. Comput. Phys. 141 (1998) 153–173.
[6] D.L. Brown, R. Cortez, M.L. Minion, Accurate projection methods for the incompressible Navier–Stokes equations, J. Comput. Phys. 168 (2001) 464–499.
[7] Y.-N. Chen, S.-C. Yang, J.-Y. Yang, Int. J. Numer. Meth. Fluids 31 (1999) 747–765.
[8] A.J. Chorin, A numerical method for solving incompressible viscous flow problems, J. Comput. Phys. 2 (1967) 12–26.
[9] W.O. Criminale, T.L. Jackson, R.D. Joslin, Theory and Computation in Hydrodynamic Stability, Cambridge University Press, 2003.
[10] F.E.C. Culick, Rotational axisymmetric mean flow and damping of acoustic waves in solid propellant rocket motors, AIAA J. 4 (1966) 1462–1464.
[11] W. E, C.-W. Shu, A numerical resolution study of high order essentially non-oscillatory schemes applied to incompressible flow, J. Comput. Phys. 110 (1993) 39–46.
[12] W.E., J. Liu, Gauge method for viscous incompressible flows, Commun. Math. Sci. 1 (2003) 317–332.
[13] U. Ghia, K.N. Ghia, C.T. Shin, High-Re solutions for incompressible flow using the Navier–Stokes equations and a multigrid method, J. Comput. Phys. 48 (1982) 387–411.
[14] P.M. Gresho, S.T. Chan, On the theory of semi-implicit projection methods for viscous incompressible flow and its implementation via a finite element method that also introduces a nearly-consistent mass matrix: part 2: implementation, Int. J. Numer. Meth. Fluids 11 (1990) 621–659.
[15] J.L. Guermond, P. Minev, Jie Shen, An overview of projection methods for incompressible flows, Comput. Meth. Appl. Mech. Eng. 195 (2006).
[16] F.H. Harlow, J.E. Welch, Numerical calculation of time-dependent viscous incompressible fluid with a free surface, Phys. Fluids 8 (1965) 2182.
[17] A.K. Henrick, T.D. Aslam, J.M. Powers, Mapped weighted essentially non-oscillatory schemes: achieving optimal order near critical points, J. Comput. Phys. 207 (2005) 542–567.
[18] F.Q. Hu, M.Y. Hussaini, J.L. Manthey, Low-dissipation and -dispersion Runge–Kutta schemes for computational acoustics, J. Comput. Phys. 124 (1996) 177–191.
[19] G.S. Jiang, C.-W. Shu, Efficient implementation of weighted ENO schemes, J. Comput. Phys. 126 (1996) 202.
[20] S.Y. Kadioglu, R. Klein, M.L. Minion, A fourth-order auxiliary variable projection method for zero-Mach number gas dynamics, J. Comput. Phys. 227 (2008) 2012–2043.
[21] K.C. Karki, S.V. Patankar, Pressure based calculation procedure for viscous flows at all speeds in arbitrary configurations, AIAA J. 27 (1989) 1167–1174.
[22] P. Moin, J. Kim, On the numerical solution of time-dependent viscous incompressible fluid flows involving solid boundaries, J. Comput. Phys. 35 (1980) 381.
[23] J. Kim, P. Moin, Application of a fractional-step method to incompressible Navier–Stokes equations, J. Comput. Phys. 59 (1985) 308–323.
[24] S.K. Lele, Compact finite differences with spectral like resolution, J. Comput. Phys. 103 (1992) 16.
[25] C.L. Merkle, M. Athavale, Time-accurate Unsteady Incompressible Flow Algorithms Based on Artificial Compressibility, AIAA Paper 87-1137, 1987.
[26] Y. Morinishi, T.S. Lund, O.V. Vasilyev, P. Moin, Fully conservative higher order finite difference schemes for incompressible flow, J. Comput. Phys. 143 (1998) 90–124.
[27] S. Nagarajan, S.K. Lele, J.H. Ferziger, A robust high-order compact method for large eddy simulation, J. Comput. Phys. 191 (2003) 392.
[28] S.A. Orszag, M. Israeli, Numerical simulation of viscous incompressible flows, Ann. Rev. Fluid Mech. 6 (1974) 281–318.
[29] S.K. Pandit, J.C. Kalita, D.C. Dalal, A transient higher order compact scheme for incompressible viscous flows on geometries beyond rectangular, J. Comput. Phys. 225 (2007) 1100–1124.
[30] S.V. Patankar, D.B. Spalding, A calculation procedure for heat, mass, and momentum transfer in three-dimensional parabolic flow, Int. J. Heat Mass Trans. 15 (1972) 1787–1806.
[31] P. Venugopal, F.M. Najjar, R.D. Moser, DNS and LES computations of model solid rocket motors, AIAA paper 2000–3571, 2000.
[32] S.E. Rogers, Numerical solution of the incompressible Navier–Stokes equations, NASA TM 102199, Ames Research Center, Moffett Field, CA, 1990.
[33] P. Spalart, Direct simulation of a turbulent boundary layer up to $Re_\theta = 1410$, J. Fluid Meek. 187 (1988) 61–98.
[34] C.C. Wu, A high order WENO finite difference scheme for incompressible fluids and magnetohydrodynamics, Geophys. Astrophys. Fluid Dynam. 101 (1) (2007) 37–61.